

SUPPLEMENTAL INFORMATION

Multimetallic Au/FePt₃ Nanoparticles as Highly Durable Electrocatalyst

Chao Wang,[†] Dennis van der Vliet,[†] Karren L. More,[‡] Nestor J. Zaluzec,[†] Sheng Peng,[§] Shouheng Sun,^{§,} Hideo Daimon,^{**} Guofeng Wang,^{††} Jeffrey Greeley,^{‡‡} John Pearson,[†] Arvydas P. Paulikas,[†] Goran Karapetrov,[†] Dusan Strmcnik,[†] Nenad M. Markovic,[†] and Vojislav R. Stamenkovic^{†,*}*

Materials Science Division, Argonne National Laboratory, Argonne, IL 60439; Division of Material Science and Technology, Oak Ridge National Laboratory, Oak Ridge, TN 37831; Department of Chemistry, Brown University, Providence, Rhode Island 02912; Technology & Development Division, Hitachi Maxell Ltd., Ibaraki 300-2496, Japan; School of Engineering, Indiana University-Purdue University, Indianapolis, IN 46202; Center for Nanoscale Materials, Argonne National Laboratory, Argonne, IL 60439

* ssun@brown.edu; vrstamenkovic@anl.gov

[†] Materials Science Division, Argonne National Laboratory

[‡] Oak Ridge National Laboratory

[§] Brown University

^{**} Hitachi Maxell, Ltd.

^{††} Indiana University-Purdue University

^{‡‡} Center for Nanoscale Materials, Argonne National Laboratory

Part 1 Methodology

Experimental Methods and Characterizations

1) Nanoparticle Synthesis

7 nm Au NPs. A solution of 10 ml 1,2,3,4-Tetrahydronaphthalene (tetralin, anhydrous 99%, Sigma-Aldrich), 10 ml oleylamine (70%, Sigma-Aldrich), and 0.1 g $\text{HAuCl}_4 \cdot 3\text{H}_2\text{O}$ (99.9985%-Au, Strem) was prepared in air at 15°C and magnetically stirred under N_2 flow. 0.5 mmol of Tert-butylamine-borane (97%, Sigma-Aldrich) complex was dissolved in tetralin (1 mL) and oleylamine (1 mL) and injected into the precursor solution. The reaction initiated instantaneously and the solution changed to a deep purple color within 5 s. The mixture was allowed to be aged at 15°C for 1 h before 60 ml acetone (ACS grade, BDH) was added to precipitate the Au NPs. The Au NPs were collected by centrifugation (8500 rpm, 8 min), washed with acetone and redispersed in hexane (ACS grade, BDH).

7/1.5 nm Au/FePt₃ NPs: 30 mg of 7 nm Au NPs were mixed with 10 ml octadecene (90%, Sigma-Aldrich), 0.1 g $\text{Pt}(\text{acac})_2$ (98%, Strem), 1 ml oleylamine and 1 ml oleic acid (90%, Sigma-Aldrich) at 120°C. 0.03 ml $\text{Fe}(\text{CO})_5$ (99.5%, Strem) was added under N_2 atmosphere, then the temperature was raised to 200°C. The solution was cooled down to room temperature after 30 minutes. 50 ml iso-propanol (99.5%, Sigma-Aldrich) was added to precipitate the NPs and the product was collected by centrifuge (6000 rpm, 5 min). The obtained Au/FePt₃ NPs were washed twice with 20 ml ethanol (denatured ACS grade, BDH) and redispersed in 10 ml hexane for further applications. Similar recipe without adding Au seeds was used to synthesize 10 nm FePt₃ NPs. Synthesized NPs were incorporated into carbon black (900 m²/g from Tanaka), and the organic surfactants were removed by heating the NPs/carbon mixture in air at 450 K for 12 h. Total metal loading was adjusted to be 20% (not including the surfactants, which occupy 19 ~ 21% wt. in the as-synthesized NPs determined by thermal gravimetric analysis) for all catalysts used in this work.

2) Material Characterizations

TEM images were collected on a Philips EM 420 (120 kV). HRTEM images were recorded using a Jeol JEM-2010 (200 kV). XRD patterns of the particle assemblies were collected on a Bruker AXS D8-Advance diffractometer with $\text{Cu K}\alpha$ radiation ($\lambda = 1.5418 \text{ \AA}$). UV/vis spectra

were recorded on a Perkin Elmer Lambda 35 spectrometer. STEM and elemental analysis were carried out on FEI Tecnai F20ST analytical electron microscopy at Argonne National Laboratory. Additional analyses were done with JEOL 2200FS TEM/STEM at Oak Ridge National Laboratory equipped with a CEOS aberration (probe) corrector. The microscope was operated at 200kV in high angle annual dark field (HAADF) scanning transmission electron microscopy (STEM) mode. The probe size was $\sim 0.7\text{\AA}$ and probe current was $\sim 30\text{pA}$ during HAADF-STEM imaging. When accumulating EDS data, to increase probe current to $\sim 400\text{-}500\text{pA}$, the probe size was $\sim 2\text{\AA}$. A Bruker-AXS X-Flash 5030 silicon drift detector was the EDS system.

3) Electrochemical Study

The catalysts were dispersed in deionized water (double-filtered, Milli-Q, $\rho \geq 18.2\text{ M}\Omega\text{-cm}$) by sonication ($>1\text{ h}$) to form $0.5\text{ mg}_{\text{cat}}/\text{ml}$ suspensions. A drop of the catalyst suspension was deposited onto a glassy carbon disk (6 mm in diameter) and dried in Ar stream. The Pt loading was $15\text{ ug}/\text{cm}^2$ (Pt/disk, controlled by amount of suspension deposited based on the Pt ratio from EDX analysis) in all cases. All cyclic voltammograms and polarization curves were recorded with sweep rates of 20 and 50 mV/s using an Autolab 302 electrochemical analyzer. 0.1 M perchloric acid (prepared by diluting ultra pure perchloric acid (70%, OmniTrace Ultra™, EMD) with deionized water) was used as the electrolyte. The prolonged potential cycling was done at 20°C in order to diminish the influence of contaminants and electrolyte evaporation, which could be significant at elevated temperatures. All potentials are given versus reversible hydrogen electrode (RHE).

4) Theory and Simulations

The DACAPO code ¹ was used for all total energy calculations in this study. A four-layer slab, periodically repeated in a super cell geometry with six equivalent layers of vacuum between any two successive metal slabs, was used; the RPBE ¹-optimized Pt₃Fe lattice constant is 3.96 Å. A (2x2) unit cell was employed. The top two layers of the slab were allowed to relax until the total force on all atoms was less than 0.04 eV/Å in any Cartesian direction. Adsorption was allowed on one of the two exposed surfaces of the metal slabs, and the electrostatic potential was adjusted accordingly ². Ionic cores were described by ultrasoft pseudopotentials ³, and the Kohn-Sham

one-electron valence states were expanded in a basis of plane waves with kinetic energy below 340 eV; a density cutoff of 500 eV was used. The surface Brillouin zone was sampled with an 18 Chadi-Cohen \mathbf{k} point grid. The convergence of the total energy with respect to the cut-off energies and the \mathbf{k} point set was confirmed. The exchange-correlation energy and potential were described by the generalized gradient approximation (GGA-RPBE)³. The self-consistent RPBE density was determined by iterative diagonalization of the Kohn-Sham Hamiltonian, Fermi population of the Kohn-Sham states ($k_B T = 0.1$ eV), and Pulay mixing of the resulting electronic density⁴. All total energies were extrapolated to $k_B T = 0$ eV.

- 1 Hammer, B., Hansen, L. B. & Nørskov, J. K. Improved adsorption energetics within density-functional theory using revised Perdew-Burke-Ernzerhof functionals. *Phys. Rev. B* 59, 7413-7421 (1999).
- 2 Bengtsson, L. Dipole correction for surface supercell calculations. *Physical Review B* 59, 12301-12304 (1999).
- 3 Vanderbilt, D. Soft self-consistent pseudopotentials in a generalized eigenvalue formalism. *Phys. Rev. B* 41, 7892-7895 (1990).
- 4 Kresse, G. & Furthmüller, J. Efficiency of ab-initio total energy calculations for metals and semiconductors using a plane-wave basis set. *Comput. Mater. Sci.* 6, 15-50 (1996).

Part 2 Electrochemical Properties of Well-Defined Surfaces

Electrochemical characterization of Pt and FePt₃ thin films on Au(111) substrate

1) Au(111)-Pt

Cyclic voltammetry of Au(111)-Pt surface in Ar saturated electrolyte does not change before and after the ORR experiments. No change in integrated charge of underpotentially deposited hydrogen (H_{upd}) demonstrates stable behavior of Pt atoms on Au substrate, confirming that surface composition stays the same.

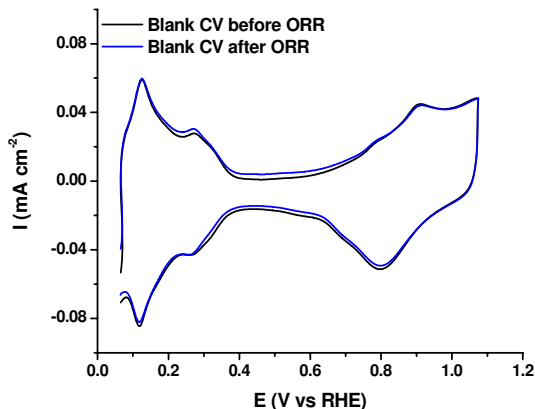


Fig. S1. Blank CV for 1.5 nm Pt thin film supported on Au(111) before (black), and after (blue) ORR measurements at 20 and 60°C. The integrated charge of H_{upd} is found to be $210 \mu\text{Ccm}^{-2}$, which is equal to the expected value for polycrystalline Pt surface.

Electrooxidation of fully covered CO adlayer over Au(111)-Pt surface revealed that integrated charge from CO stripping peak of $420 \mu\text{Ccm}^{-2}$ matches the surface area obtained from H_{upd} . That was additional confirmation that surface was fully covered with Pt atoms. In addition, cyclic voltammetry does not change before and after experiments with CO indicating that surface composition is not affected.

Fig. S2. (a) CO stripping performed on Au(111)-Pt thin film. The integrated charge of CO stripping is $420 \mu\text{Ccm}^{-2}$, which is a perfect match with expected value for polycrystalline Pt. **(b)** Blank CV measured before (blue) and after (red) CO stripping. They are similar to each other, and the H_{upd} region is identical showing no reduction in exposed Pt surface area.

2) Au(111)-FePt₃

Cyclic voltammetry of Au(111)-FePt₃ surface in Ar saturated electrolyte does not change before and after the ORR experiments, Fig. S3. The H_{upd} features are broader than in the Au(111)-Pt thin film, with the integrated charge density of $180 \mu\text{Ccm}^{-2}$, which is lower than that of Au(111)-Pt. This fits with previous results obtained on bulk alloys¹ in which H_{upd} region of Pt-bimetallic alloy surfaces was found to be lower than that of polycrystalline Pt. Additionally, no change in integrated charge of H_{upd} demonstrates stable behavior of Pt atoms on Au substrate, confirming that surface composition of Pt-bimetallic thin film stays the same.

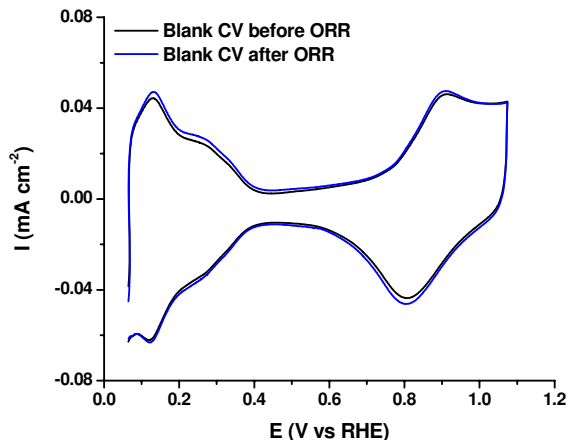


Fig. S3. Blank CV for Au(111)-FePt₃ thin film before (black) and after (blue) ORR measurements at 20 and 60°C. Similar to the Pt film on gold, from the absence of change in H_{upd} area it can be determined that there was no loss of Pt surface area during measurement of the ORR.

Electrooxidation of fully covered CO adlayer over Au(111)-FePt₃ surface revealed that integrated charge from CO stripping peak of 420 μCcm^{-2} matches the surface area obtained from Au(111)-Pt and polycrystalline Pt surfaces. The difference between integrated charges for H_{upd} and CO stripping originates from altered electronic properties of Pt topmost atoms. Due to changed electronic/adsorption properties¹ only total charge of H_{upd} is affected - decreased for about 30 μCcm^{-2} , while total coverage of CO_{ad} due to strong Pt-CO interaction remains the same as in case of pure Pt surfaces. This is additional confirmation that Pt-bimetallic thin film completely covered geometric surface area of Au(111) substrate. In addition, cyclic voltammetry does not change before and after experiments with CO indicating that surface coverage of Pt atoms stays the same.

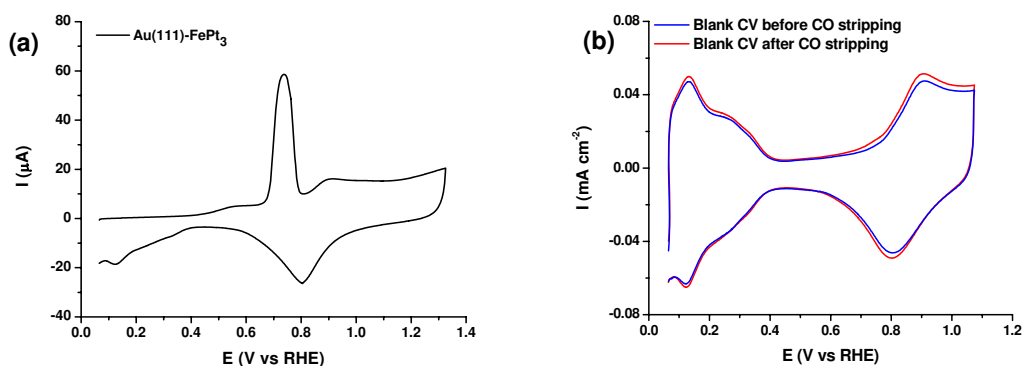


Fig. S4. (a) CO stripping performed on Au(111)-FePt₃ thin film, showing a single CO stripping feature. The integrated charge of CO stripping is 420 μCcm^{-2} , equal to the values obtained on Au(111)-Pt and polycrystalline Pt. (b) Blank CVs measured before and after CO stripping show that the H_{upd} region is identical without reduction in exposed Pt surface area.

3) The absence of Au atoms on the Au(111)-FePt₃ surface

Figure 1 in the text summarizes electrochemical characterization of well-defined extended thin film surfaces over Au(111) substrate. From this summary it is obvious that, in accordance with the electrochemical property of individual element, addition of each of these metals induces extra functionality in the catalyst. In addition, the Au surface atoms are chemically stable in acidic electrolyte and inert towards the adsorption/desorption processes of H_{upd} (region I), while reversible adsorption/desorption of surface oxides is evident in the region IV between $1.1 < E < 1.6$ V. This redox couple at 1.35 V and 1.15 V could be effectively used as a signature for the presence of Au surface atoms. In order to make systematic electrochemical analysis of these thin film surfaces, we extended potential window up to 1.65 V vs. reversible hydrogen potential. In Fig. S5, a voltammetry of Au(111)-FePt₃ which was recorded in extended potential region is given. No detectable peaks that would indicate the presence of Au were found.

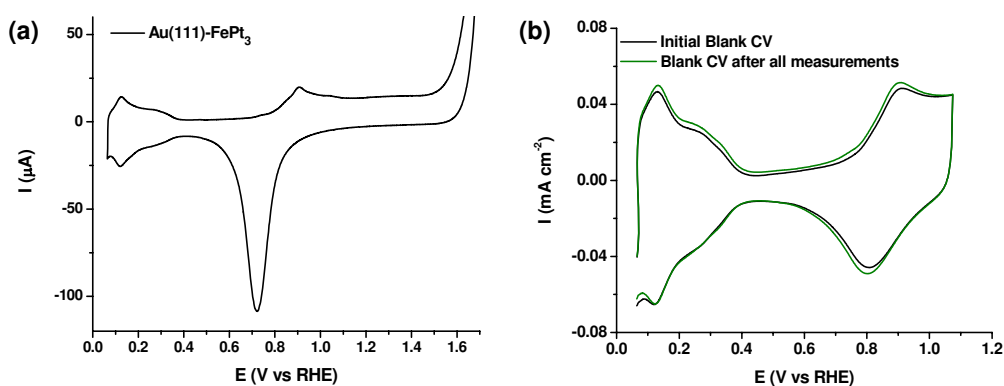


Fig. S5. (a) CV for Au(111)-FePt₃ thin film with 1.5 nm thickness by opening the potential to 1.65V. The CV does not show characteristic features for the presence of surface Au. (b) Comparison of CVs before (black curve) and after (green curve) ORR at 20 and 60°C, CO stripping and increasing the upper potential limit measurements.

In addition, comparison between CVs (Fig. S5b) before and after the whole series of electrochemical measurements such as: ORR at 20 and 60°C, CO stripping and measurements in extended potential range up to 1.65 V confirms that during the course of the measurements the H_{upd} area has not changed and the thin Pt-bimetallic film remains stable without noticeable change in surface composition.

In order to demonstrate that Au surface atoms could be detected if they are exposed to electrolyte we performed electrochemical measurements with different film thickness. Based on these results albeit was possible to conclude that surfaces of FePt₃ films that are thinner than 1 nm have some Au atoms on the surface. This is clearly visible from cyclic voltammetry in Fig. S6, in which Au redox couple is well pronounced indicating the presence of Au surface atoms. From the integrated H_{upd} charge of $170 \mu\text{Ccm}^{-2}$ it was estimated that Au surface composition was about 5%. This example confirms that this methodology can be efficiently used to detect Au surface atoms.

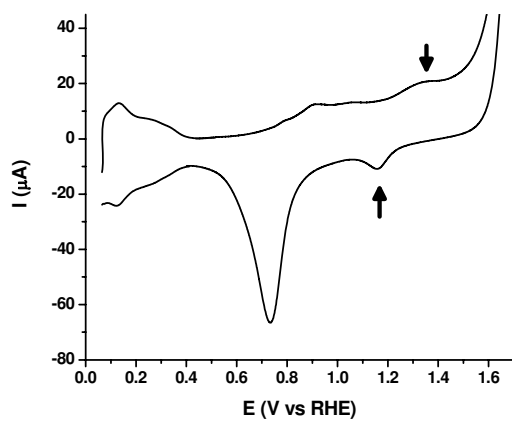


Fig. S6. CV for Au(111)-FePt₃ thin film of <1 nm by opening the potential to 1.65V. It shows clearly that, in contradictory to Au(111)-FePt₃ thin film of 1.5 nm shown above, some gold is exposed on the surface as seen by the Au-OH_{ad} redox couple at 1.35V and 1.15 V.

- 1 Stamenkovic, V. R. *et al.* Trends in electrocatalysis on extended and nanoscale Pt-bimetallic alloy surfaces. *Nature Materials* 6, 241-247 (2007).

Part 3 Properties of Multimetallic Nanoparticles

Additional characterization of the Au/FePt₃ nanoparticles

Synthetic routes for Au/FePt₃ NPs:

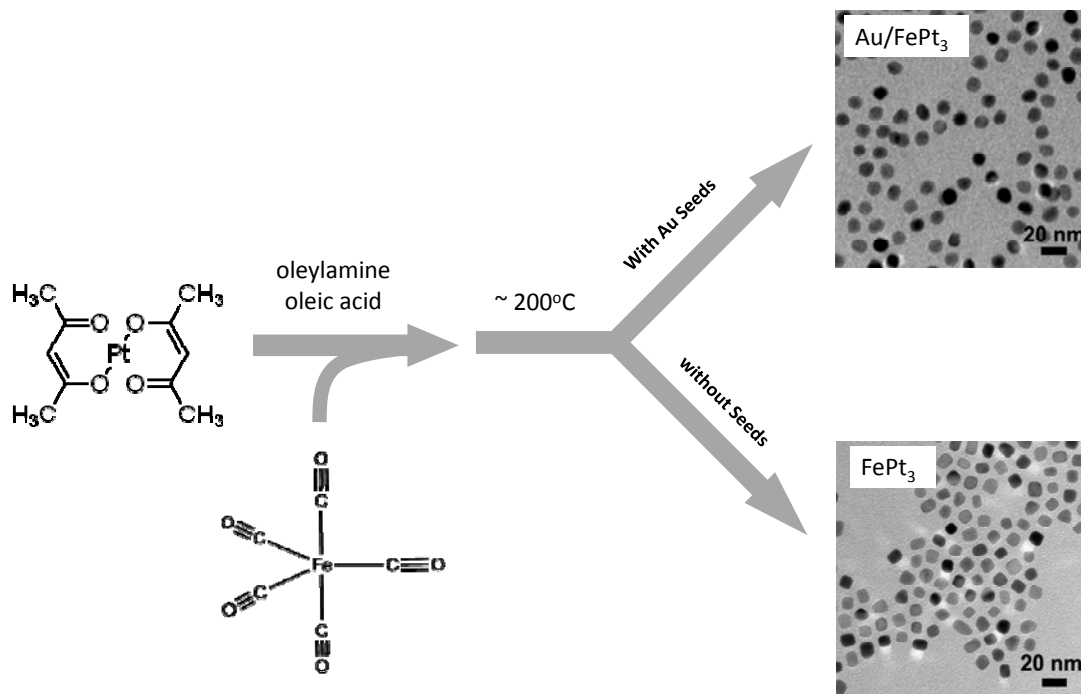


Fig. S7. Scheme of Au/FePt₃ NP synthesis. Pt(acac)₂ was thermally reduced by oleylamine to Pt, and simultaneously Fe(CO)₅ decomposed to Fe. Pt and Fe nucleated (coated) over Au seeds into Au/FePt₃ NPs. In the absence of Au seeds, FePt₃ NPs can grow under the same synthetic conditions and size can be controlled.

Elemental analysis of Au/FePt₃ nanoparticles:

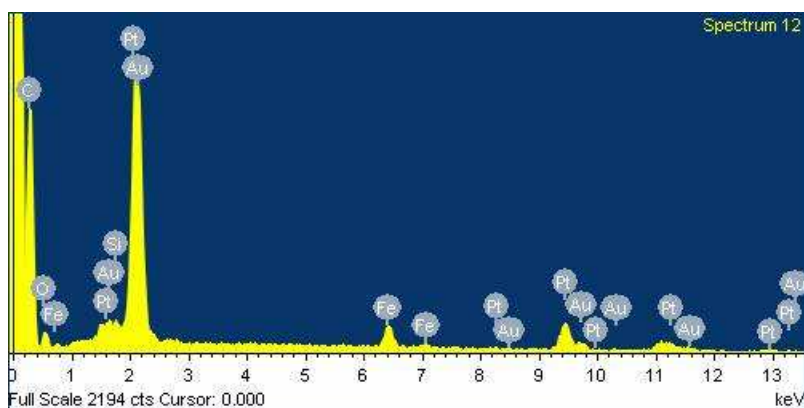


Fig. S8. EDX pattern of Au/FePt₃ NPs. The atomic composition of the NPs is Au 28%, Fe 17%, and Pt 55%.

Additional HR-TEM images of Au/FePt₃ NPs that confirm inherited shape from Au seeds

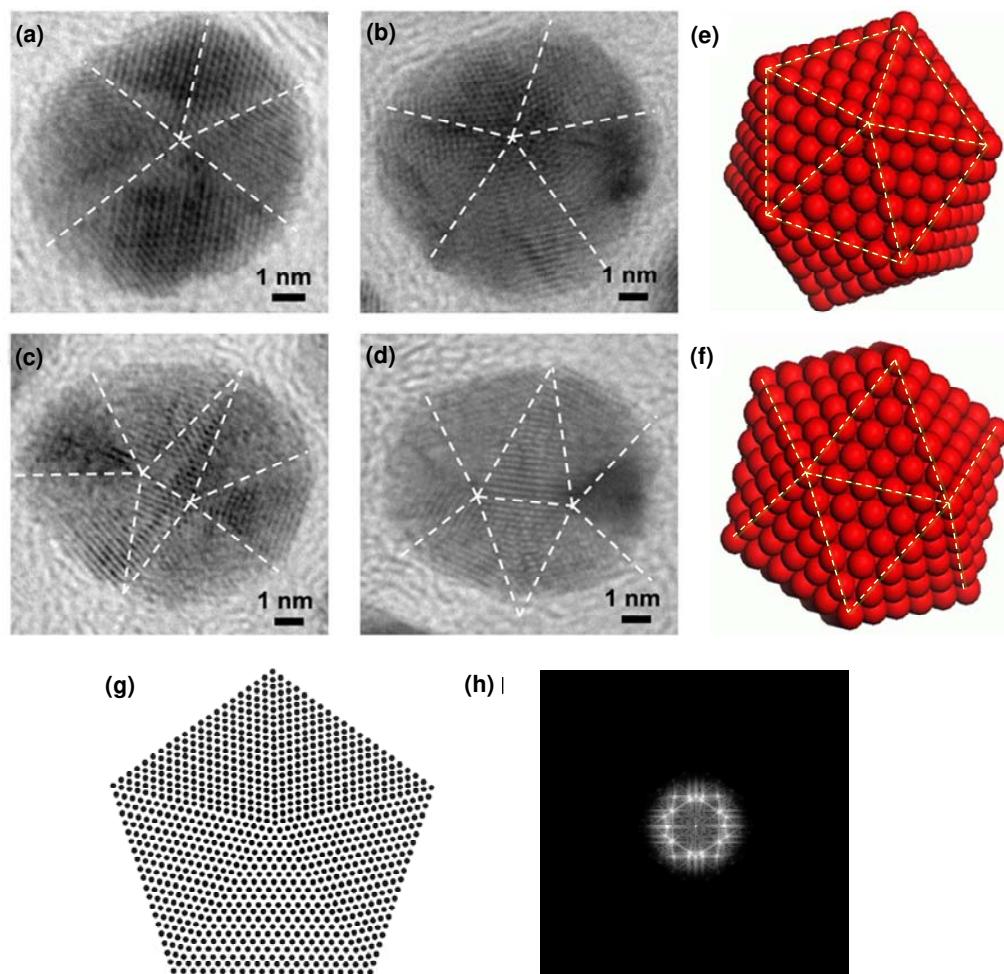


Fig. S9. (a – d) Representative HRTEM images of icosahedral Au/FePt₃ NP viewed along different directions with (e, f) the corresponding orientation of model particles. (g) The arrangement of atoms extracted from the facets around a five-fold symmetry axis of an icosahedron and (h) its FFT pattern. The multi-fold symmetry in the FFT pattern can be comparable with those shown in Fig. 2.

Elemental mapping and concentration profile of Au/FePt₃ particles

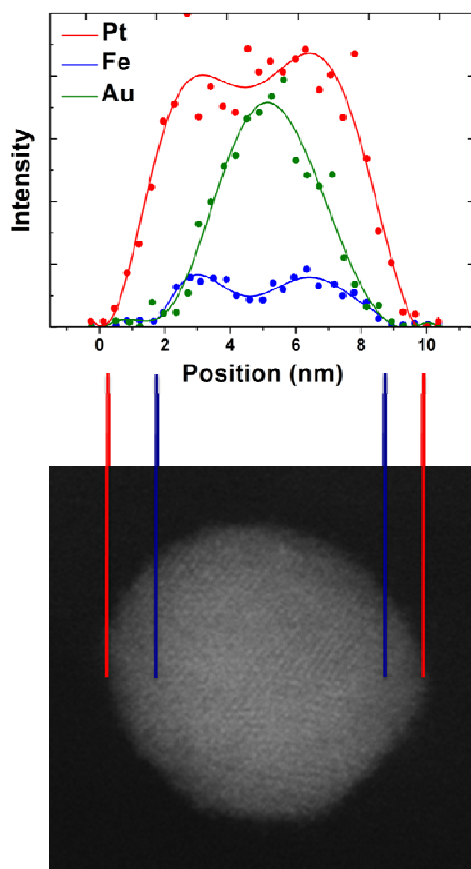


Fig. S10. More images for element mapping of Au/FePt₃ NP by HAADF-STEM. The concentration profile is clearly seen by the overlapping image (left) of Pt and Au. Below, additional line profile is given for a single Au/FePt₃ particle that reveals the coating thickness and its concentration profile.

Structural XRD analysis:

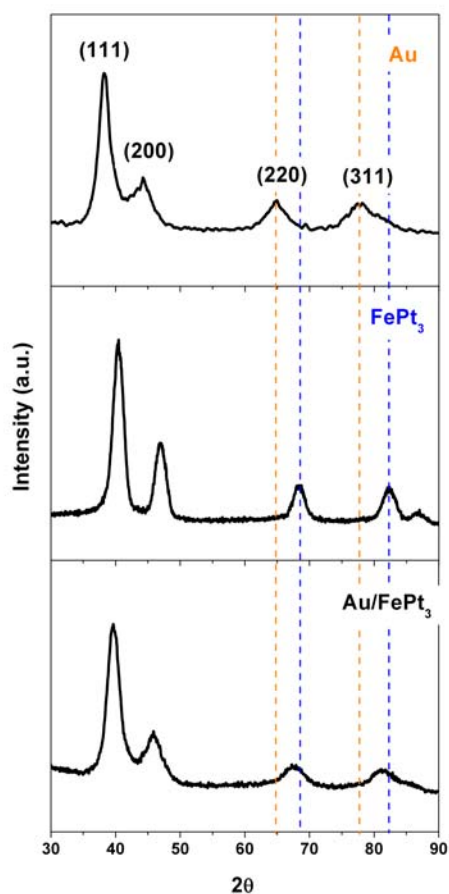


Fig. S11. Whole range of XRD patterns for Au, FePt₃, and Au/FePt₃ NPs. In addition to (111) and (200) peaks shown in Fig. 2, shift for high-angle peaks (220) and (311) are marked here (dashed lines: orange for Au, and blue for FePt₃).

Note that usually a heterogeneous core-shell structure would have broad overlaying peaks of two sets of diffraction peaks from each component in XRD, but only in the presence of several conditions. The components should have comparable amount in the whole nanostructure, as otherwise the dominant phase would bury the features of the minor phase (e.g., see the case of Pt-Au heterodimers, Wang et al., *J. Am. Chem. Soc.* 2010, 132, 6524). The two components need to show rather separate peaks so that direct overlapping is avoided (see, for example, Ag/Au core/shell nanoparticles in *J. Phys. Chem. C*, 2010, 114, 10336). A clear boundary at the interface would also be important for observing the overlaying peak, where mixed phase at the interface (interfacial alloying) would give XRD peaks between the respective peaks of each component. While all these factors may exist in the Au/FePt₃ system that lead to the absence of clear overlaying peak for Au/FePt₃, we believe the latter one plays a particularly important role, as we did observe interfacial alloying from STEM-EDX analysis (Fig. S12). The same mechanisms may apply for the other features in XRD, including the absence of Au (220) and (311) peaks in Au/FePt₃ pattern. In addition, the dominant phase in the 7/1.5 nm Au/FePt₃ particle is FePt₃, as the volume ratio of Au in is only ~34%. Similar observations were also present in our previous study on Pt-Au heterodimer nanoparticles (Wang et al., *J. Am. Chem. Soc.* 2010, 132, 6524), where the high-angle peaks of Pt in the XRD pattern for Pt-Au particles was hard to see when the size of Pt was much smaller than Au.

HAADF-STEM images that provide insight into subsurface intermixing

Interfacial alloying is observed indicating that some Au might be present in the subsurface layers

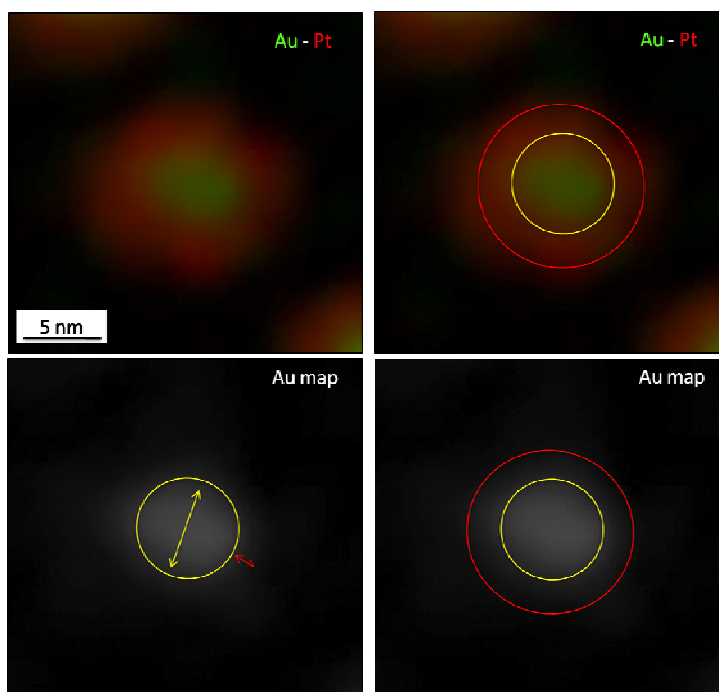


Fig. S12. HAADF-STEM analysis of the interfacial alloying in the Au/FePt₃ NPs. Au map shows ~5nm core of pure Au (yellow) and ~1 nm thick layer of mixed Au-Pt-Fe (red).

Optical properties of Au/FePt₃ NPs were investigated by UV-Vis spectroscopy and Au was not detected on the surface

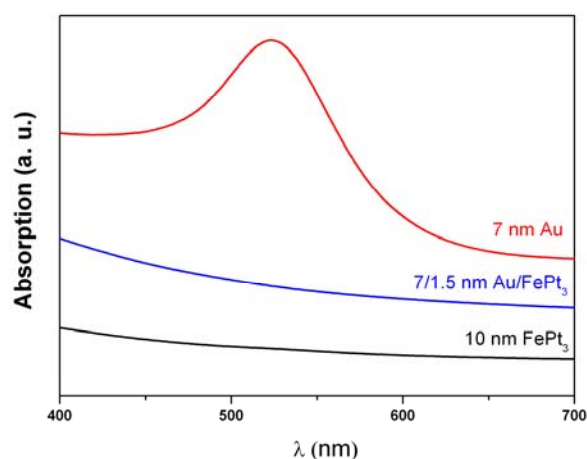


Fig. S13. UV-vis spectra of Au/FePt₃ and Au NPs dispersed in hexane. 7 nm Au NPs show a surface plasmon resonance peak around 520 nm, but Au/FePt₃ NPs have no visible feature in the UV-vis spectrum (just like FePt₃ NPs). This confirms that the Au seeds were entirely coated by FePt₃, and no Au atoms are present on the surface of multimetallic particles.

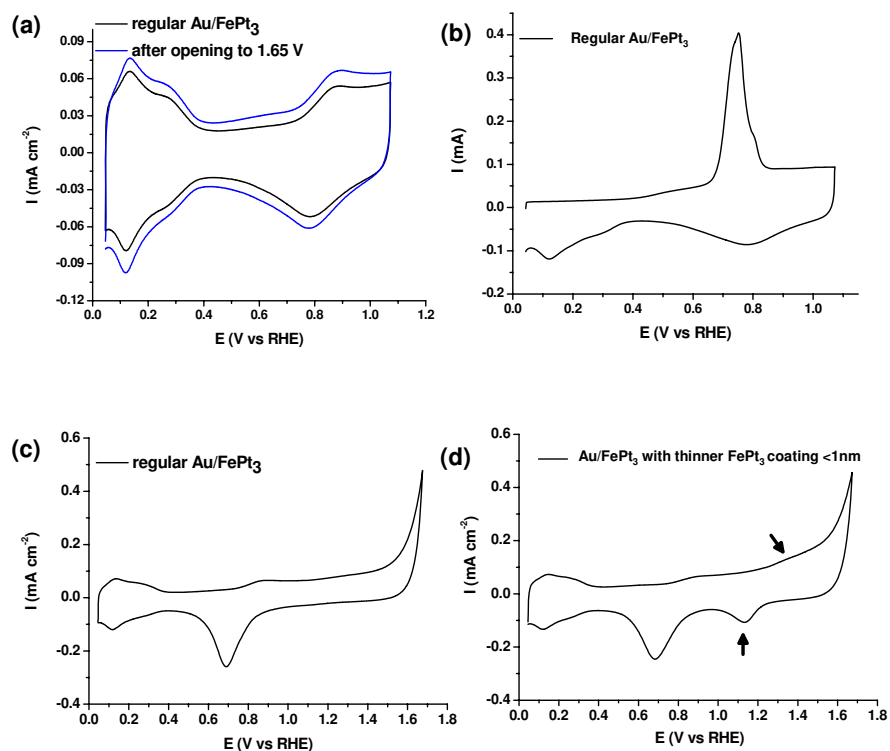


Fig. S14. Electrochemical characterization of Au/FePt₃/C nanoparticle catalyst. (a) CVs before and after electrochemical characterizations (no surface atoms of Au after opening potential to 1.65 V); (b) CO stripping curve for regular 7/1.5 nm Au/FePt₃/C NPs; (c) and (d) CVs recorded for regular and Au/FePt₃/C with thinner FePt₃ coating catalysts respectively by opening the upper potential limit to 1.65 V.

The integrated H_{upd} charge obtained from regular particles was found to be in a perfect agreement with the charge calculated from CO stripping. In Fig. S14a, CVs before and after electrochemical characterizations for ORR at 20 and 60°C, CO stripping and measurements in extended potential range up to 1.65 V confirm that during the course of the measurements the H_{upd} area has not changed and the Pt-bimetallic coating remains stable without noticeable change in surface composition. However, the double layer region has increased (blue curve in insert a) after opening and cycling potential to 1.65 V. This is due to the oxidation and consecutive roughening of the carbon support at elevated potentials. A very important finding is given in Fig. S14c, which depicts that no Au features are visible in the CV with upper potential opened to 1.65 V, confirming the formation of stable Pt surface free of any Au atoms.

We investigated another type of Au/FePt₃ NPs with bimetallic coating thickness less than 1.0 nm, which were obtained by controlled synthesis with reduced precursors (0.05 g Pt(acac)₂ and 0.015 ml Fe(CO)₅) and lower growth temperature (180°C). The particles with thinner coating, however, show characteristic gold features in the CV when the upper potential limit is opened to 1.65 V (Fig. S14d), indicating that PtM-coating does not completely encapsulate Au core. This illustrates that, if present

on the NP surface, Au atoms could be detected by cyclic voltammetry.

Additional TEM images after 60,000 electrochemical cycles.

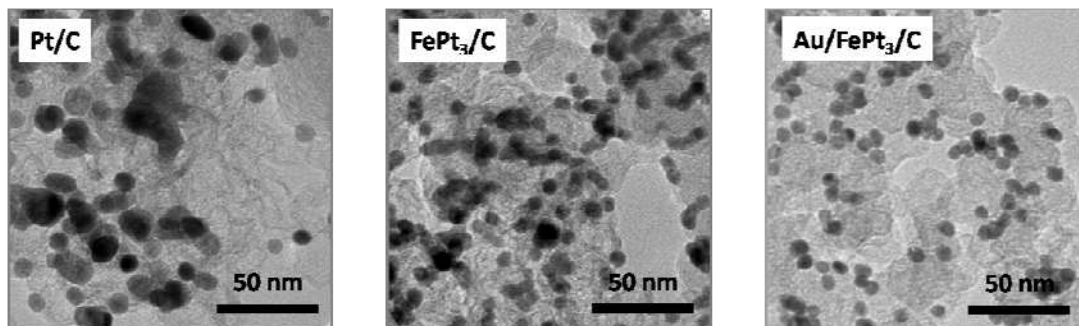


Fig. S15. More TEM images of the three catalysts after stability test. In the case of Au/FePt₃/C, though some NPs stack together, they can still be individually distinguished from each other.

Part 4 Mechanism of Stability Enhancement

1) Nanoparticle Shape

Theoretical modeling and calculation of average coordination number of surface atoms for different shape of nanoparticles

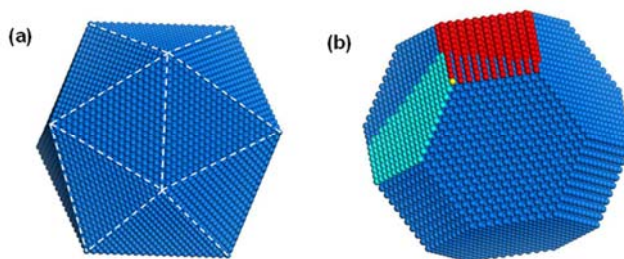


Fig. S16. The detailed analysis of the coordination number distribution of Pt surface atoms of a 10 nm NP in (a) icosahedral or (b) cubooctahedral shape. There are 29881 atoms in the cubo-octahedral NP, and 28741 atoms in the icosahedral NP. Stastical results (listed below) show that the surface of icosahedron has higher average coordination number than that of cubo-octahedron.

Coordination number	Cubo-octahedron ¹⁻³	Icosahedron ⁴
6	24	12
7	396	0
8	726	570
9	3176	3420
10	0	0
11	0	0
Total number of surface atoms	4322	4002
Average coordination number	8.632	8.849

[1] "Surface structures of cubo-octahedral Pt-Mo catalyst nanoparticles from Monte Carlo simulations", G. Wang, M.A. Van Hove, P.N. Ross, and M.I. Baskes, *The Journal of Physical Chemistry B*, 109 (2005) 11683.

[2] "Monte Carlo simulations of segregation in Pt-Ni catalyst nanoparticles", G. Wang, M.A. Van Hove, P.N. Ross, and M.I. Baskes, *Journal of Chemical Physics*, 122 (2005) 024706.

[3] "Monte Carlo simulations of segregation in Pt-Re catalyst nanoparticles", G. Wang, M.A. Van Hove, P.N. Ross, and M.I. Baskes, *Journal of Chemical Physics*, 121 (2004) 5410-5422.

[4] C.L. Cleveland and U. Landman, *J. Chem. Phys.* 94, (1991), 7376-7396.

The increase of average coordination number for icosahedral vs. cubo-octahedral particles

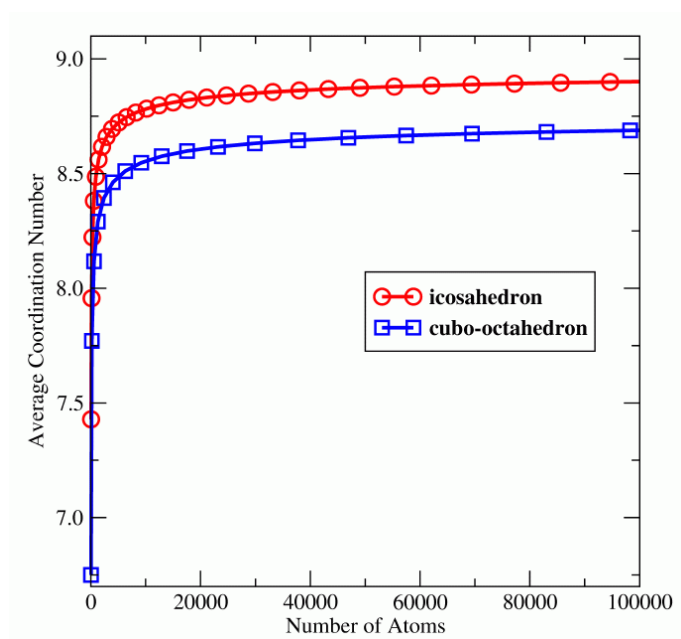


Fig. S17. Average coordination number of the surface atoms varies as a function of the total number of atoms in the particles with a cubo-octahedral, or icosahedral shape.

2) Stability enhancement through adsorbate induced segregation of Pt

Pt is much more oxophilic than Au. Pt surface atoms oxidize at more negative potentials vs. Au. The onset of oxide adsorption on Au is shifted positively for more than 600 mV (Fig. 1a).

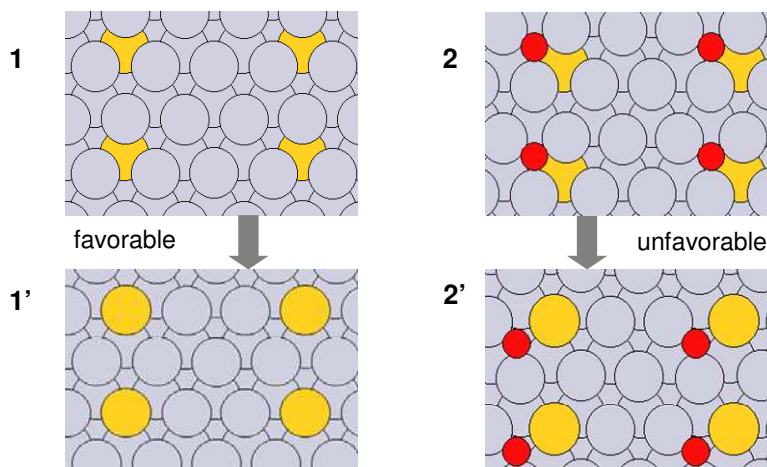


Fig. S18A. (Top view) Density Functional Theory calculations of subsurface and surface Au atoms on a Pt(111) surface: **(1-1')** A top view of Au segregation from the subsurface to the surface layer; the energy change for this process is ~ -0.4 eV in vacuum (thermodynamically favorable). **(2-2')** A top view of Au segregation from the subsurface to the surface layer in the presence of adjacent oxygen on the surface. The segregation energy in this case is ≥ 0.0 eV (thermodynamically unfavorable), and Au atoms movement to the surface is suppressed. Higher coverages of oxygen (as would be observed at elevated electrode potentials) are expected to further inhibit the movement of Au to the surface. All calculations are done on a (3×2) , 5-layer unit cell with the top three layers relaxed. The RPBE functional is used with a Monkhorst-Pack k-point grid of $(3,4,1)$; ultrasoft pseudopotentials are employed, and a planewave cutoff of 340 eV (density cutoff of 500 eV) is also used.

Gray spheres denote Pt, yellow denotes Au and red denotes O.

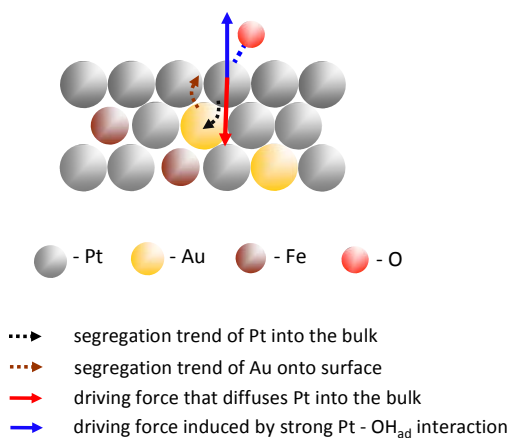


Fig. S18B. (Side View) Schematic illustration of the stability enhancement mechanism: Au atoms tend to segregate on the surface due to the lower surface energy of Au than Pt, but under the given electrochemical conditions ($0.6 < E < 1.1$ V), oxygenated species (e.g., O, OH) are strongly binding to surface Pt, which provide the driving force for Pt atoms to stay on the surface in the highly oxophilic environment. Such a counterbalance between the two opposing forces, the rather strong interaction between Pt and surface oxides on one side, and the tendency of Au to segregate over Pt on the other side, stabilizes of the topmost Pt layer.

3) Stabilization of Pt surface atoms through the hindered place exchange mechanism

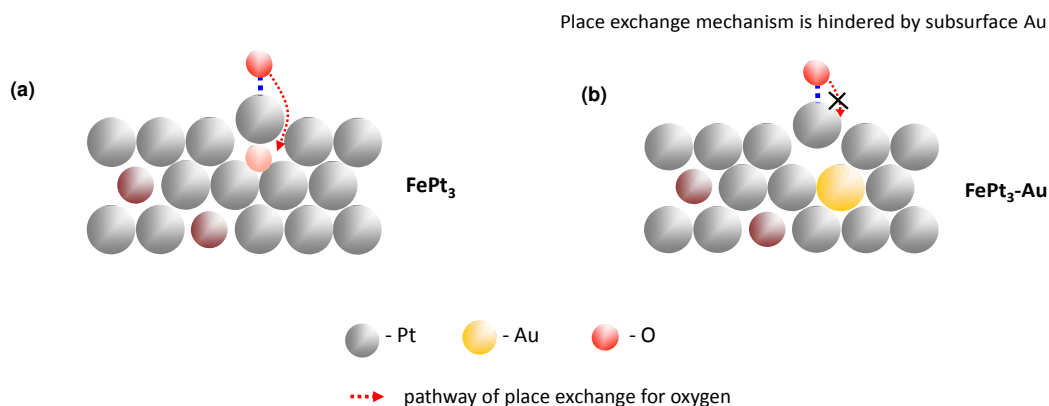


Fig. S19. (Side View) Schematic illustrations of stability enhancement mechanism of Pt surface atoms in multimetallic NPs: Au can not be oxidized in the given potential range that is relevant for the ORR ($0.6 < E < 1.2$ V), and therefore, occurrence of Au in the subsurface layers would make the formation of subsurface oxides less energetically favorable and hence suppress the dissolution of Pt.

DFT calculations of the subsurface atomic oxygen adsorption in $\text{FePt}_3(111)$ alloys with subsurface Au

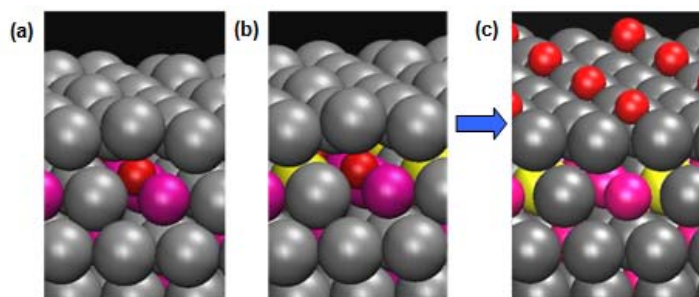


Fig. S20. (Side View) Most favorable absorption of subsurface oxygen. (a) FePt_3 alloy with 0.5 ML of Fe in the first subsurface layer, corresponding to a classic Pt skin-type structure. (b) Au/ FePt_3 alloys with 0.5 ML of Fe and 0.25 ML of Au in the first subsurface layer. When a Au atom is substituted for Pt in the subsurface layer, the strength of subsurface oxygen adsorption decreases in magnitude by about 0.15 eV. Since the corresponding strength of *surface* Pt-oxygen binding is nearly the same in both cases (c), the overall thermodynamic driving force for subsurface oxygen formation (i.e., the subsurface minus the surface oxygen binding energies) also decreases in magnitude by a comparable amount due to the presence of subsurface Au. Oxygen place exchange thus becomes thermodynamically less favorable, thereby reducing Pt loss in the ternary system under this well-known Pt-dissolution mechanism. Gray spheres denote Pt, yellow denotes Au, red denotes O, and magenta denotes Fe.